Materials Advances

ROYAL SOCIETY OF CHEMISTRY

PAPER

View Article Online
View Journal | View Issue

Check for updates

Cite this: *Mater. Adv.*, 2022, 3, 4348

$PtSe_2$ on a reduced graphene oxide foil for the alkaline hydrogen evolution reaction†

Filipa M. Oliveira, [a] Iryna Danylo, [b] Vlastimil Mazánek,[a] Martin Veselý, [b] Rui Gusmão *[a] and Zdeněk Sofer *[a]

Received 18th February 2022,
Accepted 9th April 2022

DOI: 10.1039/d2ma00190j

rsc.li/materials-advances

Reducing energy consumption during the hydrogen evolution reaction (HER) in electrocatalytic water splitting for hydrogen production is still a challenge. Among the transition metal dichalcogenide family, platinum diselenide ($PtSe_2$) exhibits good air stability, a low band-gap, and semimetallic properties, rendering it a promising catalyst for the HER. Herein, the selenization of predeposited Pt on a reduced graphene oxide (rGO) substrate forming an 88 ± 6 nm $PtSe_2$ thin layer results in a freestanding, efficient HER electrocatalyst yielding a competitive performance in an alkaline medium, achieving a low overpotential of 95 mV at −10 mA cm^{-2}. Furthermore, the $PtSe_2$/rGO foil used in a two-electrode cell configuration demonstrates good long-term stability, up to 18 hours. The performance of the $PtSe_2$/rGO foil results from the distribution of $PtSe_2$ over the rGO substrate, which is maintained after the electrochemical reactions as attested by Raman mapping, and complemented by scanning electron microscopy, inductively coupled plasma optical emission spectrometry, and X-ray photoelectron spectroscopy characterization.

Open Access Article. Published on 11 April 2022. Downloaded on 2/8/2026 10:33:00 PM.
This article is licensed under a Creative Commons Attribution-NonCommercial 3.0 Unported Licence.

Introduction

In the last few decades, society has revealed a growing concern about the use of sustainable and clean energy supplies. However, a lack of balance in the implementation of sustainable alternatives and the management of available resources, namely, traditional fossil fuels, is causing an environmental crisis. Hydrogen (H_2) has proven to be a green alternative to substitute fossil fuels and its production by water-splitting reactions has been thoroughly investigated.[1–3]

As part of the large family of two-dimensional (2D) materials,[4–6] transition metal dichalcogenides (TMDs) with a general formula of MX_2, where M stands for a transition metal (*e.g.*, Mo, Co, W, or Pt) atom sandwiched by X chalcogen atoms (S, Se or Te),[7] have great potential for realizing highly performing electrocatalysts for H_2 production through the hydrogen evolution reaction (HER).[8–10] Research on TMDs as electrocatalysts is mostly focused on Group 6 TMDs, namely, MoS_2[11,12] and WS_2.[13,14] However, limitations concerning electrical conductivity and available active sites often require extra procedures for their modification in order to improve their catalytic activity. For instance, in a recent study, Pt nanocrystals were deposited on the surface of MoS_2 edge-exposed nanoplatelets for enhancing HER performance in acidic media.[15] To overcome these limitations, and considering the multiple possibilities in the TMD family, a significant amount of research is ongoing regarding Pt dichalcogenides (PtX_2), belonging to Group 10 TMDs.[16–18] In particular, the good air stability,[19,20] low band-gap in the range of 0.21–1.2 eV,[21,22] and semi-metallic behavior[21,23] of platinum diselenide ($PtSe_2$) have incited research groups to explore its performance as a HER electrocatalyst.[23–26] It is extensively reported that a narrow band-gap is beneficial to improving the conductivity of a given material and higher carrier transmission rate, which is crucial for improving electrocatalytic performance. $PtSe_2$ can be prepared by mechanical exfoliation,[19,27] chemical vapor transport,[25,28] chemical vapor deposition,[23,29–31] selenization of Pt atoms[21] or Pt films[24] and molecular beam epitaxy,[19,32] to name a few. However, all these techniques then require the deposition of $PtSe_2$ onto an electrode support such as glassy carbon to assess its electrochemical performance. As the substrate may influence the properties of electrocatalysts due to capacitance, synergetic effects from the support, or other electrochemical features,[33] it is important to find a suitable strategy for acquiring reliable results from the electrochemical measurements. Metal-foam or metal-foil-based substrates are other approaches to support an active catalyst; however, drawbacks, such as oxidation sensitivity, limitations on large-scale production, and degradation after long-term operation are

[a] *Department of Inorganic Chemistry, Faculty of Chemical Technology, University of Chemistry and Technology Prague, Technická 5, 166 28 Prague 6, Czech Republic. E-mail: rui.gusmao@vscht.cz, zdenek.sofer@vscht.cz*

[b] *Department of Organic Technology, Faculty of Chemical Technology, University of Chemistry and Technology Prague, Technická 5, 166 28 Prague 6, Czech Republic*

† Electronic supplementary information (ESI) available. See DOI: https://doi.org/10.1039/d2ma00190j

© 2022 The Author(s). Published by the Royal Society of Chemistry

Open Access Article. Published on 11 April 2022. Downloaded on 2/8/2026 10:33:00 PM.
This article is licensed under a Creative Commons Attribution-NonCommercial 3.0 Unported Licence.

found to exist in such avenues. Therefore, the synthesis of $PtSe_2$ directly on a given substrate, thus avoiding the drop-casting technique to modify the active electrode area, could be an efficient approach to overcome the above-mentioned limitations on electrocatalyst preparation. The selection of a stable substrate such as reduced graphene oxide (rGO) could favor the production of an electrocatalyst with a scalable area, thus allowing the achievement of more reliable performance for commercial applications. In addition, the use of a flexible substrate like rGO allows easy handling during the electrocatalyst production and, later, during the HER measurements.

Hence, we produced a flexible and freestanding $PtSe_2$/rGO foil by direct selenization of a Pt film previously deposited on an rGO flexible substrate and report for the first time the HER performance in alkaline medium of $PtSe_2$ synthesized on a carbon substrate. Scanning electron microscopy (SEM) coupled with energy dispersive spectroscopy (EDS), X-ray photoelectron spectroscopy (XPS), transmission electron microscopy (TEM), X-ray diffraction (XRD), and Raman spectroscopy are used to investigate the structure and morphology of the $PtSe_2$/rGO foil. The $PtSe_2$/rGO foil is directly used for the HER in alkaline media, revealing an exceptional performance. Structural characterization after long-term stability tests shows that the overall integrity of the $PtSe_2$/rGO foil is sustained which encourages the design of Pt dichalcogenides for high-performance HER catalysis.

Materials and methods

Chemicals and materials

Platinum (99.99%) was obtained from K. J. Lesker, USA, and selenium (99.999%) was obtained from STREM, Germany. Potassium hydroxide, sulfuric acid (99.999%), and platinum nanoparticles supported on carbon with 10 and 20 wt% loading (10% Pt/C and 20% Pt/C, respectively) were purchased from Sigma-Aldrich, Czech Republic. Ruthenium(IV) oxide (RuO_2) (99.95% metal basis, Ru typically 74%) and graphite powder (2–15 μm, 99.9995%) were purchased from Alfa Aesar, Germany. A polycarbonate (PC) membrane (90 mm diameter, pore size 400 nm) was purchased from Sterlitech, USA. *N*,*N*-Dimethylformamide (DMF), phosphoric acid (85%), potassium permanganate (99%), hydrogen peroxide (30%), nitric acid (HNO_3), and hydrochloric acid (HCl) were purchased from Penta, Czech Republic. Nickel mesh (Ni mesh) (>99.8%, porosity 97%, areal density 350 g m^{-2}) and carbon paper (C_{paper}) (100%, porosity 75%, density 0.78 g m^{-3}) were purchased from Xiamen TOB New Energy Technology Co. Ltd, China. EpoFix hardener and EpoFix resin were purchased from Struers GmbH, Czech Republic.

Preparation of $PtSe_2$/reduced graphene oxide foil

The rGO foil was prepared by thermal reduction of graphene oxide (GO) prepared by assembling on a support membrane. First, the GO powder was prepared by the Tour method[34] and following the same procedure reported previously,[35] in which 3 g of graphite was stirred in a solution of concentrated sulfuric acid (98 wt%, 360 mL) and phosphoric acid (85 wt%, 40 mL). The mixture was allowed to cool to 0 °C, and afterward, 18 g of potassium permanganate, $KMnO_4$, was added to the reaction mixture, whereafter the mixture was stirred for 1 h and allowed to reach room temperature. Then, the reaction mixture was heated to 50 °C for 6 h and left to cool to room temperature and stirred for 12 h. Subsequently, the reaction mixture was poured into a flask containing 400 g of ice and 10 mL of hydrogen peroxide (H_2O_2). The unreacted $KMnO_4$ and manganese dioxide were removed by adding 20 mL of H_2O_2. The reaction mixture was allowed to settle and then decanted. Finally, the GO was purified by repeated centrifugation and multiple washes in deionized water followed by a final vacuum drying. Afterward, the obtained GO was dispersed in water (1 mg mL^{-1}), of which 100 mL was filtered through a PC membrane, and dried in an oven at 60 °C for 24 h. The GO foil was mechanically removed from the PC template and reduced by heating at 800 °C in a hydrogen (H_2) atmosphere (heating rate of 1 °C min^{-1}, a duration of 2 h, H_2 gas flux of 100 mL min^{-1}). For the synthesis of $PtSe_2$ on the rGO foil, a 60 nm thick layer of platinum (Pt) was first evaporated (at a pressure of 1×10^{-5} mbar) onto an rGO foil using an e-gun vacuum evaporator. Subsequently, the Pt/rGO foil was placed in a two-zone furnace. First, the Pt/rGO foil was heated at 650 °C in an argon (Ar) gas flow (99.9999%, 250 mL min^{-1}), and afterward, the selenium (Se) source was heated in the second zone at 250 °C. The treatment proceeded for 2 hours and the furnace was freely cooled to room temperature. A schematic illustration of the synthesis of $PtSe_2$ on the rGO foil is shown in Scheme 1.

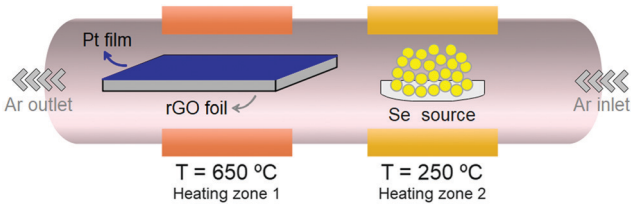

Scheme 1 Illustration of the $PtSe_2$ synthesis on an rGO foil.

Structural and morphological characterization

The morphology of the materials was investigated using SEM with a FEG electron source (Tescan Lyra dual-beam microscope). The measurements were carried out using 8 and 10 kV accelerating voltages, depending on the samples: 8 kV for surface analysis of the $PtSe_2$/rGO foil and 10 kV for cross-section analysis of the resin mold. EDS was used for elemental composition and mapping using an 80 mm^2 SDD detector (Oxford Instruments) and AZtecEnergy software. The measurements were carried out using 8, 10, or 20 kV accelerating voltages, depending on the samples. For SEM and EDS analyses of the surface morphology and respective elemental composition, the samples were directly placed on carbon tape. For cross-section analysis by SEM and EDS, the already measured $PtSe_2$/rGO foil by SEM was fastened to a plastic holder in

Open Access Article. Published on 11 April 2022. Downloaded on 2/8/2026 10:33:00 PM.
This article is licensed under a Creative Commons Attribution-NonCommercial 3.0 Unported Licence.

such a way that the microstructure along the foil thickness and length was accessible for imaging. The assembly was put into a plastic cup, serving as a container for epoxy resin, with an inner diameter of 25 mm. The container volume was filled with the resin prepared prior to the filling by mixing EpoFix Resin and EpoFix Hardener in the weight ratio of 25 to 3, respectively. After 24 h of hardening at a temperature of 60 °C, the resin block was removed from the plastic cup, and the surface of the hardened block was ground and polished. Before the SEM analysis, the polished surface was coated with a 5 nm gold layer to ensure electrical conductivity.

High-resolution (HR) XPS (HR-XPS) was performed using an ESCAProbeP spectrometer (Omicron Nanotechnology Ltd, Germany) with a monochromatic Al X-ray radiation source (1486.7 eV). The samples were placed on conductive carbon tape and HR scans of Pt 4f and Se 3d were collected. A low-energy e-gun was used to eliminate sample charging during the measurement (1–5 V).

TEM was performed using an EFTEM Jeol 2200 FS microscope (Jeol, Japan) at an acceleration voltage of 200 keV, assisted by the selected area electron diffraction (SAED) technique. Pictures were taken using an SIS MegaView III digital camera (Soft Imaging Systems) and analyzed using AnalySIS v. 2.0 software. Elemental maps were acquired using an X-MaxN 80 TS SDD detector from Oxford Instruments (England). For sample preparation, the material was lightly scraped from the as-prepared $PtSe_2$/rGO foil on the $PtSe_2$ side and dispersed in DMF. The suspension was drop-cast on a TEM grid (Cu, 200 mesh, Formvar/carbon from TED PELLA, Inc.) and dried overnight in a vacuum oven at 50 °C.

An InVia Raman microscope (Renishaw, England) was used for Raman spectroscopy measurements in backscattering geometry with a CCD detector. A Nd:YAG laser (532 nm wavelength) and a 20× objective were used for data collection. Instrument calibration was achieved using a silicon reference, which gave the peak position at 520 cm^{-1} and a resolution down to 1 cm^{-1}. The laser power used for these measurements was 1 mW. Mapping scans were collected with pixel sizes of 6.2 μm × 6.2 μm and the individual Raman spectra were batch-processed using our routine written in MATLAB. For every single spectrum, routine (I) smooths the raw spectrum using a nonparametric method removing noise with preserving signal intensity, routine (II) identifies and corrects the baseline of the smoothened spectrum, routine (III) identifies the number of peaks in the range of Raman shift between 140 and 260 cm^{-1}, and routine (IV) fits the baseline-corrected spectrum with a number of Gaussian peaks, which equals the number of identified peaks. Then, the fitted peaks around the Raman shift of 180 cm^{-1} and 209 cm^{-1} were used to plot maps showing the homogeneity of the $PtSe_2$/rGO foil on the $PtSe_2$ side for peak intensity, peak intensity ratio, and exact Raman shifts. Details of the used routine are included in the ESI.†

XRD measurements were carried out using a Bruker D8 Discoverer (Bruker, Germany) diffractometer in Bragg–Brentano parafocusing geometry under Cu Kα radiation (λ = 0.15418 nm, U = 40 kV, I = 40 mA). The diffraction patterns were collected at room temperature for 2θ values from 10 to 60°. The data were evaluated using HighScore Plus 4.9 software.

Electrothermal vaporization (ETV) coupled with inductively coupled plasma optical emission spectrometry (ICP-OES) was used to determine the wt% Pt elemental composition of the as-prepared $PtSe_2$/rGO foil and $PtSe_2$/rGO foil after a long-term stability test. The measurements were carried out using a Spectro ARCOS spectrometer (SPECTRO Analytical Instruments, Germany). For sample preparation, a representative 4 to 5 mg of sample was dissolved in 4 mL of a mixture of concentrated HNO_3 and HCl in a 1 : 3 volume ratio using a hot plate. After the dissolution process, the dissolute was cooled, filtered, diluted with deionized water, and transferred to a clean vial prior to analysis.

Electrochemical characterization

Electrochemical measurements were done at room temperature using an Autolab PGSTAT204 (Eco Chemie, Utrecht, The Netherlands) controlled by NOVA Version 2.1.4 software. Glassy carbon (GC) electrodes with a diameter of 3 mm (CH Instruments, Texas, USA), and $PtSe_2$/rGO foil, rGO foil, carbon paper (C_{paper}), and Ni mesh, all of them with an area of 0.9 cm^2, were used as working electrodes (WE); a carbon rod was used as a counter electrode and Ag/AgCl/Sat. KCl was used as a reference electrode (CH Instruments, Texas, USA). Suspensions of 10% Pt/C (1.5 mg mL^{-1} in DMF), 20% Pt/C (1.5 mg mL^{-1} in DMF), and RuO_2 (1 mg mL^{-1} in deionized water) were used for WE modification. The C_{paper} and Ni mesh were modified with 10% Pt/C and RuO_2, respectively. For 10% Pt/C@C_{paper}, the modification was done by drop-casting 20 μL of 10% Pt/C suspension onto both surfaces (20 × 2 μL, total mass loading of 66.7 μg cm^{-2}) of the C_{paper} and drying under air for 3 h. The RuO_2@Ni mesh catalyst was prepared by following the same process by drop-casting 30 μL of RuO_2 suspension onto both surfaces (30 × 2 μL, total mass loading of 66.7 μg cm^{-2}) of the Ni mesh. The modification of the GC WE was done by drop-casting 3 μL of 10% Pt/C (total mass loading of 63.4 μg cm^{-2}) and 20% Pt/C (total mass loading of 63.4 μg cm^{-2}) on it. The assembly of $PtSe_2$/graphene foil, C_{paper}, and Ni mesh as WEs was carried out as follows: the WEs were cut into rectangular pieces with a dimension of 0.5 × 1.5 cm. For each WE, the respective rectangular piece was attached to a platinum plate electrode clamp (Gaoss Union, China) and then the active surface area corresponding to 0.9 cm^2 was immersed into the electrolyte. For the modification of C_{paper} and Ni mesh, the 10% Pt/C and RuO_2 suspensions were drop-cast on the corresponding 0.9 cm^2 active area.

Double-layer capacitance (C_{dl}) measurements were carried out in a non-faradaic region. The scan rate varied within the range of $20 < \nu < 200$ mV s^{-1}, and $0.9 < E < 1.3$ V *vs.* reversible hydrogen electrode (RHE). The C_{dl} values of each electrode were extracted from the slope of the dependence of the current density ($\Delta I_a - I_c$) on the scan rate, at a fixed potential of +1.1 V *vs.* RHE (for further details see the ESI†). The electrochemical impedance spectroscopy (EIS) response of each

© 2022 The Author(s). Published by the Royal Society of Chemistry

Open Access Article. Published on 11 April 2022. Downloaded on 2/8/2026 10:33:00 PM.
This article is licensed under a Creative Commons Attribution-NonCommercial 3.0 Unported Licence.

electrode was measured at −0.08 V *vs.* RHE at a frequency ranging from 0.1 Hz to 1 MHz and an amplitude of 10 mV.

Linear sweep voltammetry (LSV) measurements were performed in a three-electrode cell configuration at 2 mV s^{-1} and the potentials were converted to the RHE using the Nernst equation, $E_{RHE}(V) = E_{Ag/AgCl} + 0.059pH + E^0_{Ag/AgCl}$, in which $E^0_{Ag/AgCl}$ = 0.197 V *vs.* standard hydrogen electrode (SHE). Cyclic voltammograms (CVs) of the $PtSe_2$/rGO foil were obtained at a scan rate of 100 mV s^{-1} between η_{20} and +0.3 V *vs.* RHE, for 100, 1000, and 3000 cycles. The long-term stability experiments were conducted in: (i) a three-electrode cell configuration with the $PtSe_2$/rGO foil for 120 min at a constant current density of −10 mA cm^{-2}. The rGO foil was tested under the same conditions for comparison; and in (ii) a two-electrode cell configuration with the $PtSe_2$/rGO foil as the cathode and Ni mesh-RuO_2 as the anode for 18 h at a constant current density of 10 mA cm^{-2}. For comparison, the same conditions were used for C_{paper} (cathode)‖Ni mesh (anode) and 10% Pt/C@C_{paper} (cathode)‖RuO_2@Ni (anode) cell configurations. All electrochemical experiments were carried out in 1.0 M KOH solution without iR compensation.

Results and discussion

Morphological and structural characterization of the $PtSe_2$/rGO foil

The $PtSe_2$/rGO foil was prepared by the direct selenization of Pt, which was previously deposited on an rGO foil by physical vapor deposition as illustrated and described in the Experimental section. Fig. 1(a) shows the visual aspect of the $PtSe_2$/rGO foil, capable of sustaining torsion. From the SEM micrographs at low magnification, it is observable that the surface of the foil on the $PtSe_2$ side is filled with irregularities, wrinkles, and plateaus from the foil (Fig. 1b and c). As shown in Fig. 1(d), at higher magnification, the $PtSe_2$ side is abundant in submicron particles with an average size of 145.0 ± 48.1 nm. Fig. 1(e) shows a histogram of the particle size distribution fitted by a Gaussian curve on the $PtSe_2$ side. The ratio of each element was measured by EDS, as shown in Fig. 1(f) and Table S1 (ESI†), confirming the successful selenization of Pt as the expected stoichiometry was obtained, that is ≈1 for the metal (Pt) and ≈2 for the chalcogenide (Se). From the elemental mapping by EDS (Fig. S1, ESI†), a homogeneous distribution of the Pt and Se elements on the $PtSe_2$ side is observed, additional evidence of the effectiveness of the method used in the production of the $PtSe_2$/rGO foil. The EDS spectrum (Fig. 1f) reveals the energy signals associated with Pt and Se, whereas the rGO side attests that only carbon and oxygen are present. Morphological analysis was also performed by TEM and SAED, coupled with EDS elemental mapping (Fig. S2, ESI†). The TEM image (Fig. S2a, ESI†) shows clusters of $PtSe_2$ particles, and from the details of the $PtSe_2$ surface by HR-TEM (Fig. S2b, ESI†) regular lattice fringes are observed with a *d*-spacing of 0.5385 nm (Fig. S2c, ESI†), thus suggesting the formation of a layered structure. The corresponding SAED pattern (Fig. S2d, ESI†) evidenced the crystalline structure of the as-synthesized $PtSe_2$ on rGO foil. The EDS elemental mapping (Fig. S2e, ESI†) revealed that both Pt and Se elements are homogeneously distributed, and non-coincidental with the mapping of the C element.

In the Raman spectrum of the $PtSe_2$ side of the foil (Fig. 1g), two prominent peaks with similar intensity are observed at 179.7 and 209.0 cm^{-1} assigned, respectively, to E_g and A_{1g} modes.[36] These values are in agreement with previous studies on Raman characterization of $PtSe_2$ materials.[28,37,38] From the Raman spectrum on the rGO side (Fig. 1g), it is evident that only carbon is present, as the vibrational modes of $PtSe_2$ were not observed. The full Raman spectrum of the rGO side is shown in Fig. S3(a) (ESI†), with a weak D band at 1339 cm^{-1} and a very intense G band at 1582 cm^{-1}, indicating a high level of crystallinity of the graphene formed by the reduction of the GO foil. A magnification of the spectrum is shown in Fig. S3(b) (ESI†). Included in Fig. S5 (ESI†) is the Raman spectrum of the GO foil with D- and G-bands at 1344 and 1598 cm^{-1}, respectively. By comparing the GO and rGO foil spectra, it is noticed that there is a significant decrease in the D band intensity in the rGO foil due to the highly effective reduction of GO during the heat treatment at 800 °C. Such a reduction removed the oxygen groups in the GO, thus increasing the surface area of rGO.

The XRD diffractogram of the $PtSe_2$ film on the $PtSe_2$ side is shown in Fig. 1(h1–h3), and the crystallographic data agree with the hexagonal structure of $PtSe_2$ with $P\bar{3}m1$ (164) space group and lattice constants of $a = b$ = 3.728 Å and c = 5.081 Å.[16] According to the powder diffraction file (PDF) no. 00-050-1574, the peaks at 17.4, 45.4, 48.9 and 52.1° can be ascribed, respectively, to the (001), (102), (110) and (111) crystal planes of $PtSe_2$. The magnification of Fig. 1(h1) in the 16–19° (Fig. 1h2) and 43–53° (Fig. 1h3) 2θ ranges shows these peaks more clearly. The peaks at 26.4° (002), 44.5° (101) and 54.6° (004) are associated with the rGO substrate together with corresponding $K\beta$ diffraction peaks at 23.9 and 25.4°.

To characterize the cross-section of the $PtSe_2$/rGO foil, we embedded the material in epoxy resin, let the epoxy harden, and grounded and polished the epoxy block. The complete cross-section shown in Fig. 2(a) reveals the entire thickness of the prepared foil of 71.5 ± 4.1 μm, as well as the thickness of the $PtSe_2$ layer of 88 ± 6 nm, which is shown in detail in Fig. 2(b). Fig. 2(b) further shows the red arrow, alongside which an EDS elemental mapping was acquired. The elemental profiles show clear Gaussian distributions with full width at half maximum (FWHM) values of 109 nm and 136 nm for Pt and Se, respectively (Fig. 2c and d), which confirms the thin character of the $PtSe_2$ layer at the top of the foil. Furthermore, Pt and Se evince a high positive spatial correlation with a Pearson coefficient of 0.986. This infers that a spot with a high Pt concentration also has a high Se concentration. Complementary to the Pt and Se profiles, carbon was measured as well. The spatial correlation of Pt–C and Se–C evinces negative correlation coefficients of −0.8978 and −0.9026, respectively. The value means that where the concentration of Pt or Se is high, the concentration of C is low, and *vice versa*.

Open Access Article. Published on 11 April 2022. Downloaded on 2/8/2026 10:33:00 PM.
This article is licensed under a Creative Commons Attribution-NonCommercial 3.0 Unported Licence.

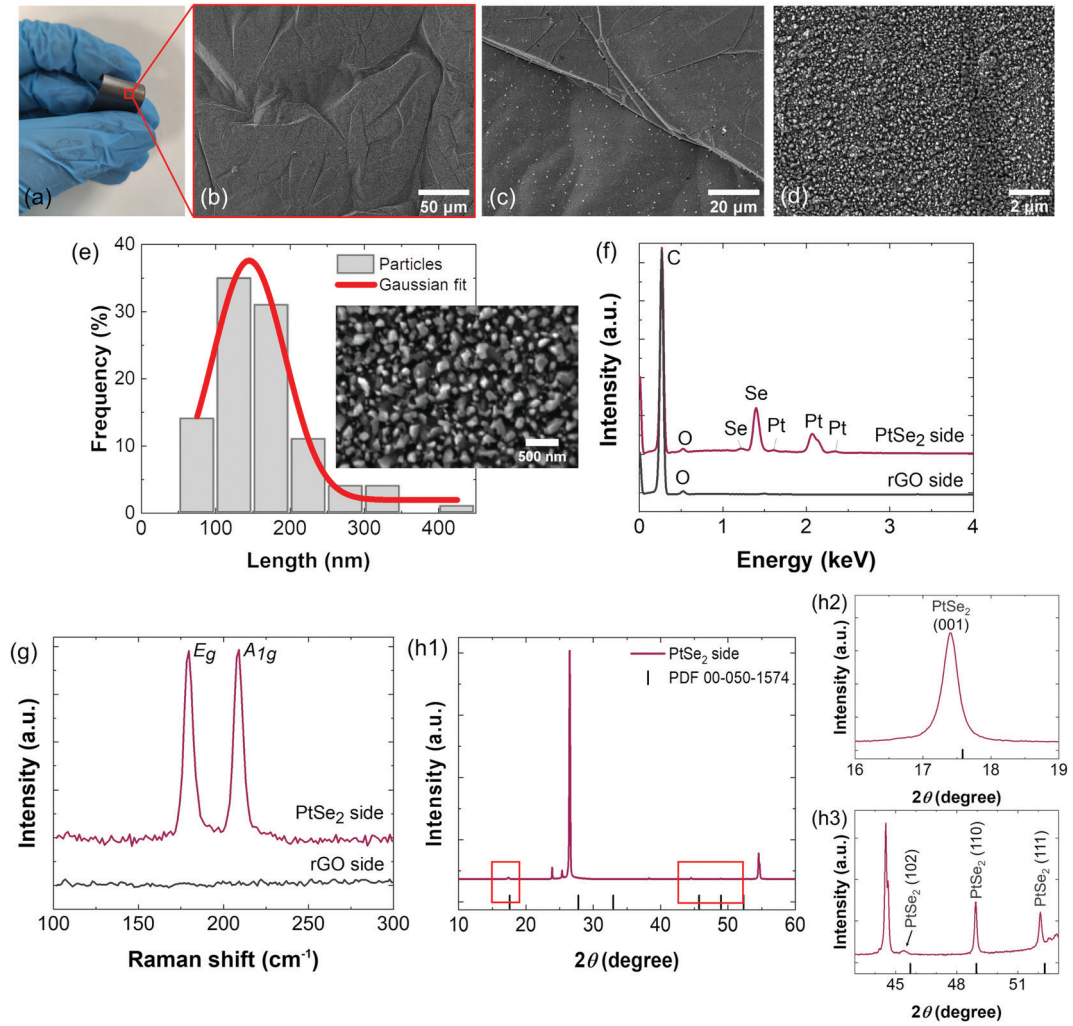

Fig. 1 Characterization of the $PtSe_2$ foil. (a) Photograph of the $PtSe_2$ foil on the $PtSe_2$ side, and the respective (b–d) SEM micrographs at different magnifications. (e) Particle-size distribution on the $PtSe_2$ side. (f) The EDS spectrum from mapping of elements of the $PtSe_2$ foil on both sides. (g) Raman spectra of the $PtSe_2$ foil on both sides. (h1) XRD diffractogram on the $PtSe_2$ side with magnifications in (h2) 16– 19° and (h3) 43–53° ranges.

Furthermore, the atomic ratio of Pt/Se alongside the whole line probe is constantly close to the value of 0.5, which also equals the stoichiometry of $PtSe_2$ on the $PtSe_2$ side.

$PtSe_2$/rGO as an electrocatalyst for the HER

To evaluate the HER performance, the $PtSe_2$/rGO foil was initially tested in a three-electrode cell in an alkaline (1.0 M KOH) electrolyte by LSV at a sweep rate of 2 mV s^{-1}. The LSV polarization curves are shown in Fig. 3(a) and it is seen that in the first LSV, an overpotential of 95 mV was necessary to reach the current density of −10 mA cm^{-2} (η_{10}). After 100 continuous cyclic voltammograms (CVs) at 100 mV s^{-1}, a difference of only 19 mV in the η_{10} was observed (Fig. 3a).

As these results indicate that the $PtSe_2$/rGO foil has excellent performance for the HER under alkaline conditions, its electrocatalytic activity was further evaluated and compared with that of the commercial benchmark catalyst 10% Pt/C deposited on GC (10% Pt/C@GC). In Fig. S4 (ESI†), an optical image of C_{paper} (Fig. S4a, on the left, ESI†) and its morphology by SEM (Fig. S4b, ESI†) are shown. The typical LSV curves are illustrated in Fig. 3(b) and the numeric results are included in Table S2 (ESI†). Unmodified C_{paper} and rGO are included for comparison and they were revealed to be unstable in alkaline media, reaching a η_{10} of 552 and 850 mV, respectively, in the first scan. The LSV curves of the WEs modified with 10% Pt/C show their typical performance as HER electrocatalysts in alkaline media. However, the η_{10} at 191 mV for 10% Pt/C@GC, represents a value of 96 mV, higher compared to that of the fabricated $PtSe_2$/rGO foil. Moreover, the commercial 20% Pt/C deposited on GC (20% Pt/C@GC) yielded an η_{10} value of 157 mV (Fig. 3b and Table S2, ESI†), which confirms the superior catalytic activity of the $PtSe_2$/rGO foil.

To further assess the performance of the $PtSe_2$/rGO foil, the HER kinetics was evaluated based on the Tafel slopes determined from the corresponding LSV curves, shown in Fig. S5a (ESI†) and summarized in Table S2 (ESI†). The Tafel slope for the $PtSe_2$/rGO foil is 120 mV dec^{-1}, which is lower than that of 10% Pt/C@GC (152 mV dec^{-1}). On the other hand, the Tafel

© 2022 The Author(s). Published by the Royal Society of Chemistry

Open Access Article. Published on 11 April 2022. Downloaded on 2/8/2026 10:33:00 PM.
This article is licensed under a Creative Commons Attribution-NonCommercial 3.0 Unported Licence.

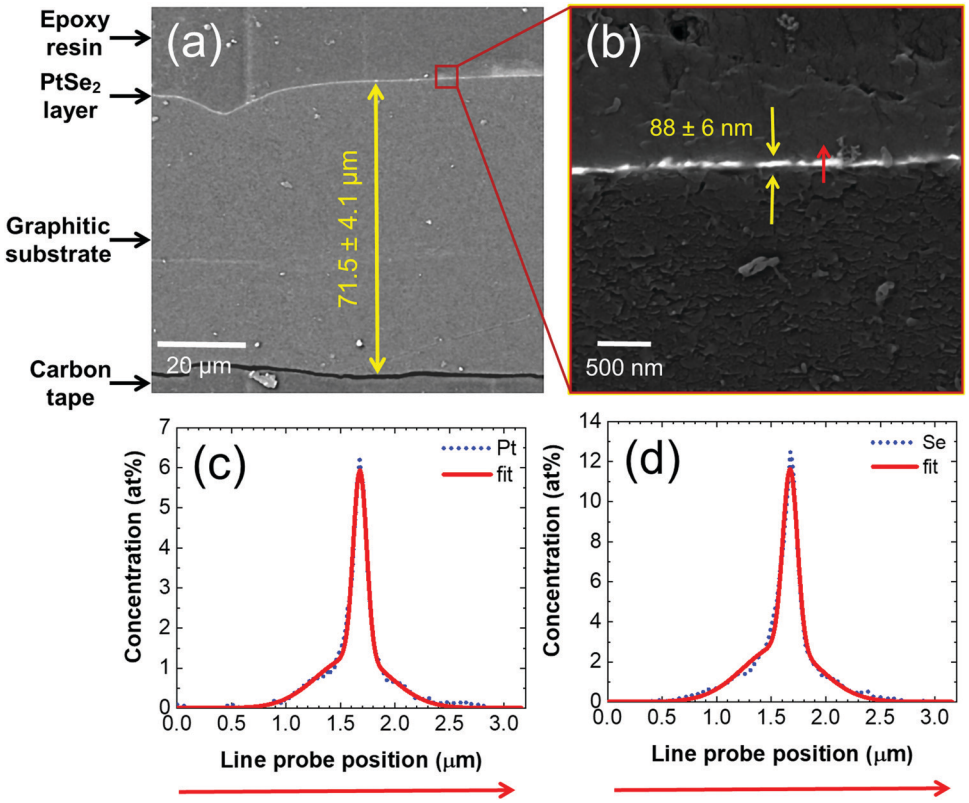

Fig. 2 (a) Polished cross-section SEM image of the material revealing both the thickness of the $PtSe_2$ film and the rGO substrate. (b) Detailed microstructure of the $PtSe_2$/rGO foil showing the thickness of the $PtSe_2$ film. The red arrow denotes an EDS elemental line probe for (c) Pt and (d) Se elements.

slope of 20% Pt/C@GC was 100 mV dec^{-1} (Fig. S5a and Table S2, ESI†). Despite these lower Tafel slope values compared to those of the $PtSe_2$/rGO foil, a favorable kinetic process on the $PtSe_2$/rGO foil can be stated as it requires less energy for water dissociation. Moreover, it is suggested that the adsorption equilibria follow a Volmer–Heyrovský pathway as the Tafel slope value is in the range of 40–120 mV dec^{-1}.[10]

Moreover, a correlation between the Tafel slope and η_{10} is shown in Fig. 3(c), and it is seen that the direct selenization of Pt is advantageous for the HER activity because the $PtSe_2$/rGO foil has a comparable kinetics process to that of 10% Pt/C@GC but requires a lower η_{10} (Fig. 3 and Table S2, ESI†), the recommended parameter for evaluating the HER efficiency. As mentioned above, the $PtSe_2$/rGO foil has a higher Tafel slope value compared to that of 20% Pt/C@GC (Fig. 3 and Table S2, ESI†), but since these three materials fall within a similar rate-determining step (RDS) *i.e.*, the Volmer–Heyrovský mechanism, improvements are expected in the catalytic activity of the $PtSe_2$/rGO foil.

The Pt mass activity was determined within the potential range studied, as shown in Fig. S5c (ESI†), reaching a value of 48 mA mg_{Pt}^{-1} @ −0.10 V *vs.* RHE. The turnover frequency (TOF)[39] was also determined for the different potentials, as shown in Fig. S5d (ESI†), reaching a maximum of 0.45 s^{-1} @ −0.57 V *vs.* RHE.

The general trend in the catalytic performance of the materials under study is maintained, *i.e.*, $PtSe_2$/rGO foil > 20% Pt/C@GC > 10% Pt/C@GC > C_{paper}. Also included in Table S2 (ESI†) is the electrocatalytic performance of some metal diselenide and platinum catalysts for the HER in KOH reported in the literature. As observed, the HER performance of the $PtSe_2$/rGO foil in alkaline media yields competitive values compared to those of 10% Pt/C and other Pt-based materials.

Furthermore, the electrocatalytic stability of the $PtSe_2$/rGO foil was assessed before and after 1000 CVs, aiming to determine the overpotential at a current density of −100 mA cm^{-2} (η_{100}). In addition to the $PtSe_2$/rGO foil remaining stable until reaching the desired current (−100 mA cm^{-2}), again, there is a slight shift of about 20 mV in the η_{100} after 1000 CVs, stabilizing at 591 mV, as shown in Fig. 3(d). However, worse $PtSe_2$/rGO foil performance was verified with additional cycling, after 3000 CVs; the η_{10} increased to 280 mV and the η_{100} reached 725 mV, as shown in Fig. S5b (ESI†).

To further understand the role of $PtSe_2$ in the improved HER performance of the $PtSe_2$/rGO foil, the electrochemical double-layer capacitance (C_{dl}) and charge transfer resistance (R_{ct}) were evaluated. The C_{dl} value is obtained by plotting the capacitive currents from the cyclic voltammetry (CV) curve as a function of the scan rates at a selected potential,[40] in a non-faradaic region, as shown in Fig. 4(a) and respective CVs in Fig. S6(a–c), with further details given in the ESI.† The CV measurements were performed at various scan rates, from 20 to 200 mV s^{-1}, with the calculated C_{dl} values of $PtSe_2$/rGO at 1.1 V *vs.* RHE being much higher than those of the other materials (Fig. S6d, ESI†),

Open Access Article. Published on 11 April 2022. Downloaded on 2/8/2026 10:33:00 PM.
This article is licensed under a Creative Commons Attribution-NonCommercial 3.0 Unported Licence.

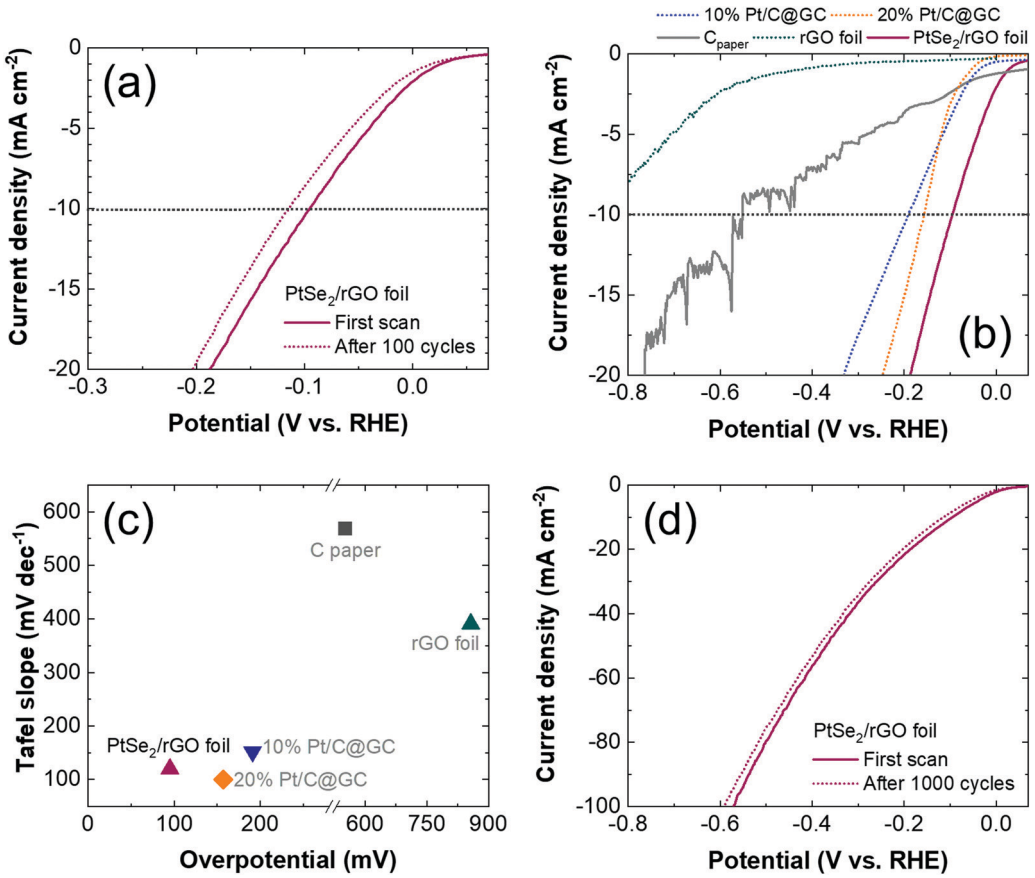

Fig. 3 HER performance in 1.0 M KOH. (a) LSV polarization curves of $PtSe_2$/rGO foil. (b) Comparison of $PtSe_2$/rGO foil LSV polarization curves with those of other catalysts and (c) the corresponding correlation between Tafel slope and overpotential at −10 mA cm^{-2}. (d) Polarization curves of the $PtSe_2$/rGO foil before and after 1000 cycles. Scan rate: 2 mV s^{-1}.

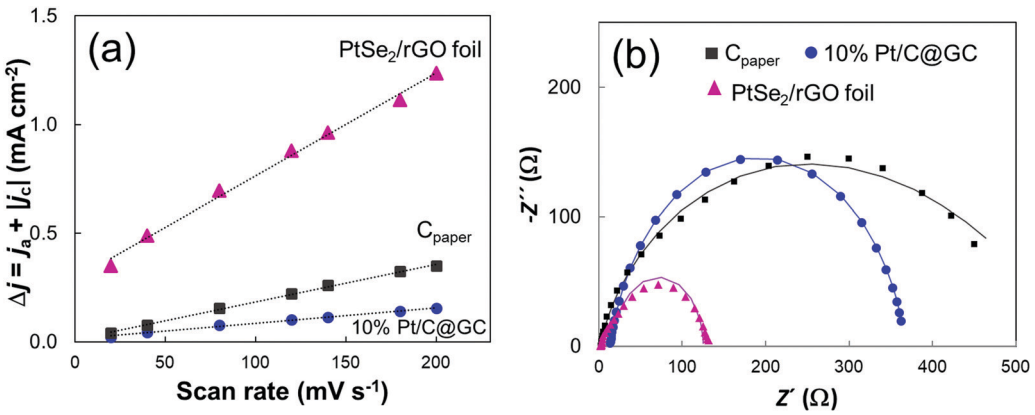

Fig. 4 (a) Plots of the capacitive current density at 1.1 V *vs.* RHE for the determination of C_{dl} and (b) the respective Nyquist plot for the determination of R_{ct} of materials at −0.05 V *vs.* RHE. The fitting of the Nyquist experimental curves is shown as a continuous line. Tested materials: C_{paper}, 10% Pt/C@GC, and $PtSe_2$/rGO foil.

thus implying a larger electrochemically accessible surface area and higher concentration of active sites.

EIS measurements were performed to estimate electrode kinetics, with lower R_{ct} being associated with a faster reaction rate. The respective Nyquist plots of the materials are shown in Fig. 4(b), as well the fitted curves from which R_{ct} values were determined. The R_{ct} value of $PtSe_2$/rGO of 105 Ω still was lower than that of C_{paper} and 10% Pt/C@GC.

Next, the long-term stability of the $PtSe_2$/rGO foil was investigated in the chronopotentiometric mode by maintaining

© 2022 The Author(s). Published by the Royal Society of Chemistry

Open Access Article. Published on 11 April 2022. Downloaded on 2/8/2026 10:33:00 PM.
This article is licensed under a Creative Commons Attribution-NonCommercial 3.0 Unported Licence.

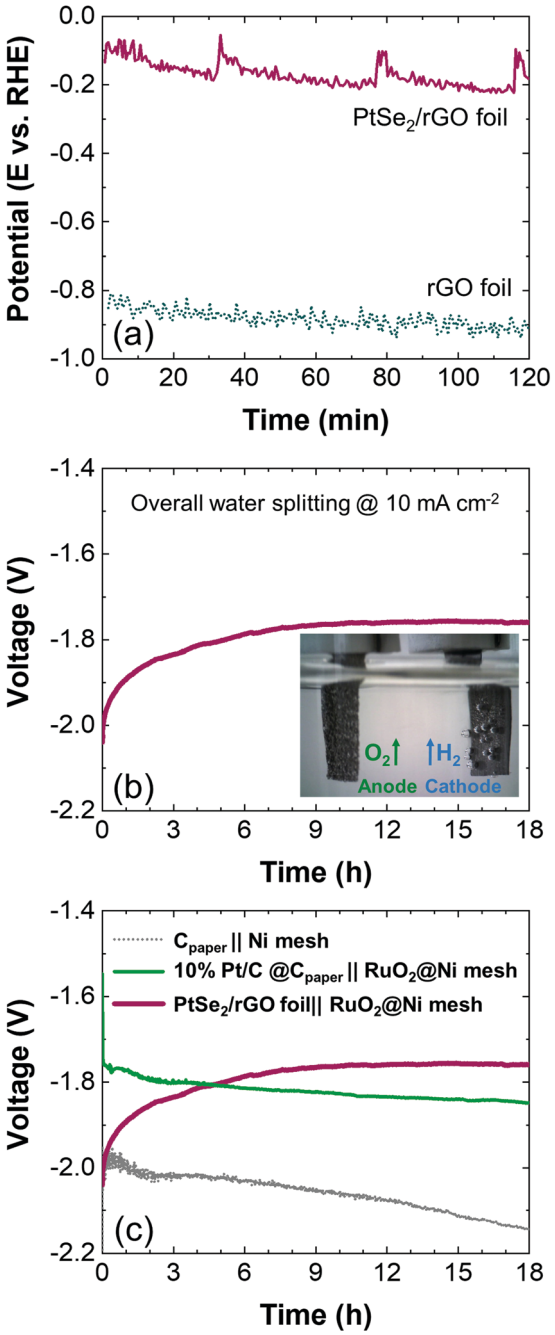

Fig. 5 Long-term stability HER tests by chronopotentiometry in 1.0 M KOH. (a) Chronopotentiometric curves of the $PtSe_2$/rGO foil compared with the rGO foil electrolyzers at a fixed current of −10 mA cm^{-2} for 120 min in a three-electrode configuration. (b) Chronopotentiometric curve of $PtSe_2$/rGO foil‖RuO_2@Ni mesh at a fixed current density of 10 mA cm^{-2} for 18 h in a two-electrode configuration. The respective setup is shown in the inset. (c) Chronopotentiometric curves of different alkaline electrolyzers compared with $PtSe_2$/rGO foil‖RuO_2@Ni mesh.

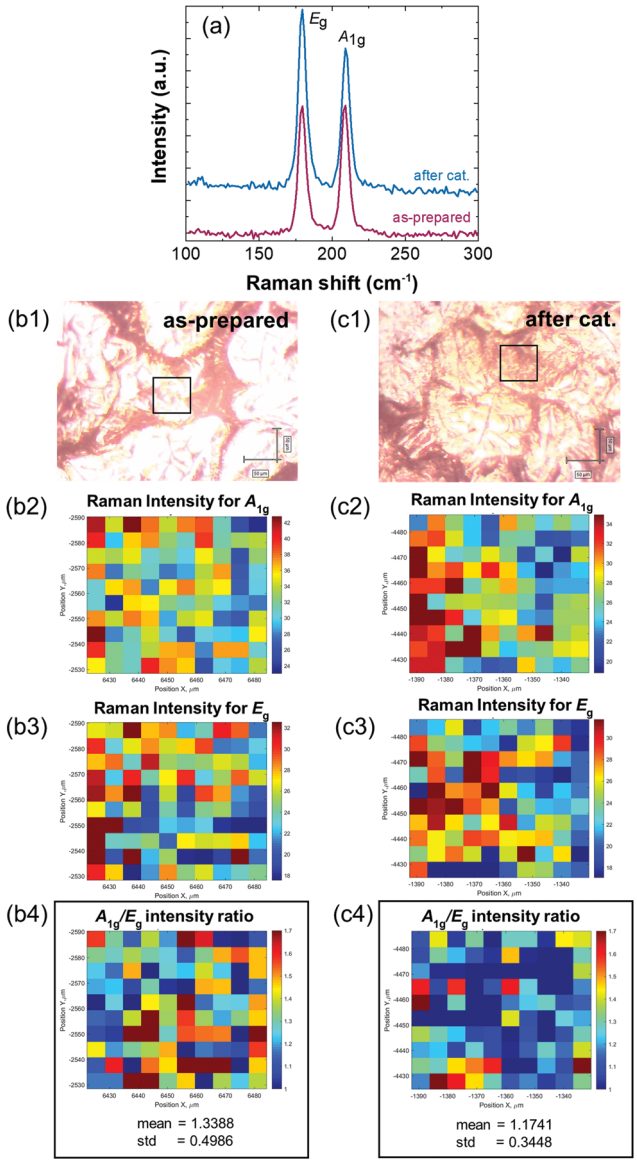

Fig. 6 Raman characterization of the $PtSe_2$/rGO foil on the $PtSe_2$ side. (a) Raman spectra of the as-prepared samples and samples after long-term stability tests. Photographs of (b1) as-prepared samples and (c1) samples after long-term stability tests acquired using a Raman microscope. Mapping of (b2–b4) as-prepared samples and (c2–c4) samples after long-term stability tests. The 50 × 50 μm image was acquired from the black rectangle in the photographs. The corresponding 10 × 10 pixels maps show the spatial distribution of A_{1g} and E_g vibrational mode intensities and the ratio of the A_{1g}/E_g signal, which points out the degree of $PtSe_2$ exfoliation both for the as-prepared and used $PtSe_2$/rGO foil on the $PtSe_2$ side. The mean value of A_{1g}/E_g characterizes a global degree of exfoliation, while the standard deviation value indicates the exfoliation degree homogeneity within the mapped area.

a constant current density of −10 mA cm^{-2} for 120 min. The corresponding response is shown in Fig. 5(a) and it is compared with that of the rGO foil. The $PtSe_2$/rGO foil performs better when compared to the rGO foil after 120 min as the first one requires an average potential of −162 mV *vs.* RHE while −883 mV *vs.* RHE is necessary for the latter in order to sustain −10 mA cm^{-2}. This improvement in stability in the $PtSe_2$/rGO foil suggests greater robustness of this electrode conferred by the selenization procedure.

To obtain a complete profile of the stability of the $PtSe_2$/rGO foil, long-term tests were performed by chronopotentiometry for 18 h at a fixed current of 10 mA cm^{-2}, as the current density of −10 mA cm^{-2} is accepted as the benchmark to compare

Open Access Article. Published on 11 April 2022. Downloaded on 2/8/2026 10:33:00 PM.
This article is licensed under a Creative Commons Attribution-NonCommercial 3.0 Unported Licence.

electrocatalytic materials for the HER.[41] Instead of a conventional three-electrode configuration, its performance was tested in a two-electrode cell, as it is the configuration used commercially. The $PtSe_2$/rGO foil was used as the cathode and for the anode, RuO_2, a benchmark catalyst for the OER,[42] was deposited on Ni mesh (RuO_2@Ni mesh) as described in the Experimental section. Fig. S7(a) (ESI†) shows the LSV curves towards the OER for Ni mesh and RuO_2@Ni mesh samples, and the chronopotentiometric response of the RuO_2@Ni mesh sample at a fixed current of -10 mA cm^{-2} over 18 h in a three-electrode configuration is presented in Fig. S7(b) (ESI†). In Fig. S4(a) (ESI†) (on the right) an optical image of the Ni mesh and its morphology is shown by SEM (Fig. S4f, ESI†) as well as the morphological and elemental characterization after modification with RuO_2 (Fig. S4g–i, ESI†). A comparison with C_{paper} after modification with 10% Pt/C as the cathode is also included, and its morphological and elemental characterization is shown in Fig. S4(c–e) (ESI†).

The corresponding chronopotentiometric curve in a two-electrode configuration is shown in Fig. 5(b), and the inset exhibits gas bubbling as evidence of electrolysis. The $PtSe_2$/rGO foil reaches a plateau, being stable at a voltage of -1.76 V by the end of the stability test (18 h). By comparing with other alkaline electrolyzers in the same two-electrode configuration (Fig. 5c), the setup with the benchmarks Pt/C and RuO_2 (10% Pt/C@C_{paper}‖RuO_2@Ni mesh) revealed a stable performance over time but requires a higher voltage (-1.85 V) to sustain the current. The stability curve of the configuration with the unmodified electrodes, *i.e.*, C_{paper}‖Ni mesh, shows major instability over time and decreased performance, and therefore, a higher voltage is required (-2.14 V).

Structural characterization after the HER

To assess the integrity of the $PtSe_2$/rGO foil on the $PtSe_2$ side after electrochemical tests, it was subject to characterization by Raman spectroscopy, SEM, ICP-OES, and XPS. Fig. 6(a) compares the Raman spectra of the $PtSe_2$/rGO foil before and after long-term stability tests. Both E_g and A_{1g} vibration modes can be observed with no Raman shift deviations, *i.e.*, the two peaks are centered at 179.7 and 209.0 cm^{-1}. A visual comparison between the as-prepared and the used $PtSe_2$/rGO foil on the $PtSe_2$ side is shown in Fig. S8(a and b) (ESI†), respectively. From Fig. S8(b) (ESI†) it can be noticed that there is some loss of the active material in restricted sections of the film, but more importantly, holes or punctures are absent, thus the overall integrity of the foil is sustained. This evidence that the $PtSe_2$ foil maintains its integrity after electrolysis was confirmed by SEM after long-term stability tests, and is shown in Fig. S8(c1–c3) (ESI†). The micrographs of the resulting EDS

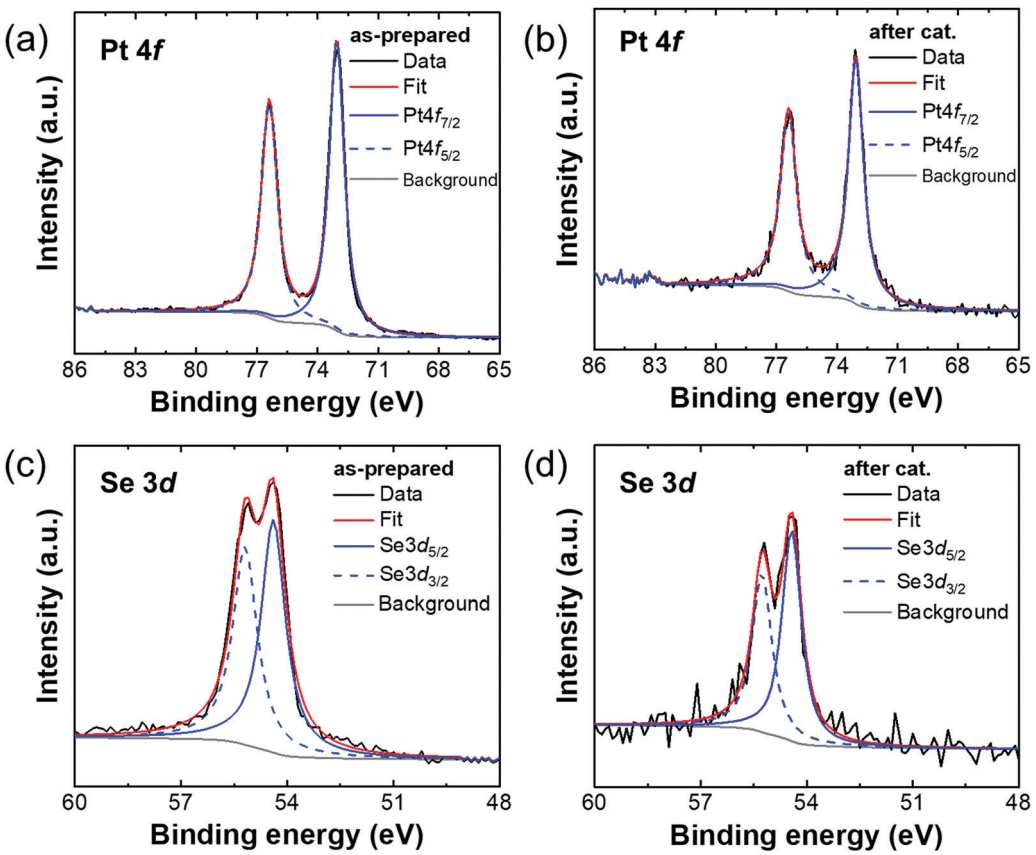

Fig. 7 XPS spectra of core levels: (a and b) Pt 4f and (c and d) Se 3d with respective deconvolution of peaks and assignment of components for the $PtSe_2$ foil on the $PtSe_2$ side. Left- and right-hand spectra are for as-prepared samples and samples after long-term stability tests, respectively.

© 2022 The Author(s). Published by the Royal Society of Chemistry

Open Access Article. Published on 11 April 2022. Downloaded on 2/8/2026 10:33:00 PM.
This article is licensed under a Creative Commons Attribution-NonCommercial 3.0 Unported Licence.

elemental mapping (Fig. S8e, ESI†) show that the distribution along the surface of the Pt and Se elements is maintained.

The $PtSe_2$ side of the foil, both for as-prepared and used (after electrochemistry), was mapped using a Raman microscope in the area of 50 × 50 μm (Fig. 6b1–c4) to determine the spatial distribution of Raman A_{1g} and E_g vibrational modes of $PtSe_2$. Intensities of these vibrational modes are dependent on the number of layers in the exfoliated $PtSe_2$,[32] where A_{1g} intensity denotes the out-of-plane stretching of Se atoms. Therefore, the A_{1g}/E_g intensity ratio value increases with the number of layers in $PtSe_2$. Thus, Raman mapping provides information about the degree of exfoliation within the explored area and the exfoliation spatial homogeneity. To access these quantities, individual Raman spectra were independently processed to smoothen the signal (Fig. S9a, ESI†), detect and remove the spectrum background (Fig. S9b, ESI†) and fit the smoothed and background-corrected spectrum with a set of Gaussian functions (Fig. S9c, ESI†). After this, the Gaussian parameters describing the A_{1g} and E_g vibrational modes were used for the determination of the peak position and peak intensity. Both A_{1g} and E_g intensity values are very homogeneous within the mapped area. However, the A_{1g} intensity values, which denote the out-of-plane stretching of Se atoms, reach for the foil after the long-term stability test around 80% of A_{1g} intensity values for the as-prepared foil, although the E_g intensity values remain almost the same for both foils. As a result of map combination, the A_{1g}/E_g intensity ratio for the foil after the long-term stability test (Fig. 6c4) shows homogeneously distributed lower values than those of the as-prepared foil (Fig. 6b4).

The C_{dl} of the used $PtSe_2$/rGO foil after catalysis was also monitored, as shown in Fig. S5(f) (ESI†) in which a decrease of *ca.* 9% was obtained. Thus, the foil subjected to prolonged HER did not have a significant loss in its electrochemical surface area.

By ICP-OES analysis a Pt content of about 0.087 wt% was measured, which is further evidence of the stability of the catalyst as the value measured before the long-term stability test was 0.088 wt%.

Hence, XPS spectra (Fig. 7) were measured to monitor the chemical stability of the $PtSe_2$/rGO foil before and after the long-term stability test. Pt 4f (Fig. 7a and b) was deconvoluted with a pair of peaks for $PtSe_2$ at a binding energy of 73 eV for the Pt $4f_{7/2}$ component and with a spin–orbit splitting of 3.33 eV. The core level Se 3d (see Fig. 7c and d) was also deconvoluted with pair of peaks representing selenide at binding energies of 54.4 and 55.2 eV for Se $3d_{5/2}$ and Se $3d_{3/2}$ components, respectively. Except for components assigned to $PtSe_2$, no other bonding states can be observed for the as-prepared and used $PtSe_2$/rGO foil, which further confirms its stability during the long-term experiment.

Conclusions

In this paper, we have reported the successful selenization of predeposited Pt on a freestanding rGO foil. The produced $PtSe_2$/rGO foil behaves as an efficient and stable electrocatalyst for the hydrogen evolution reaction in alkaline media as it reached an η_{10} of 95 mV, having a rate-determining step related to the Volmer–Heyrovský mechanism. In the long-term stability test, a voltage of −1.76 V was sustained at the end of 18 h when tested in a two-electrode cell at 10 mA cm^{-2}. After the long-term stability tests, no Raman shift deviations were noticed for the characteristic vibration modes of $PtSe_2$, confirming its stability as a HER catalyst in an alkaline medium. Furthermore, ICP-OES results reveal that the amount of Pt is not significantly reduced in the used $PtSe_2$/rGO foil, with the XPS also pointing to no major shifts in the binding energies and the oxidation state of the Pt and Se elements.

Conflicts of interest

There are no conflicts of interest to declare.

Acknowledgements

This project was supported by Czech Science Foundation (GACR No. 20-16124J). M. V. acknowledges the European Structural and Investment Funds, OP RDE-funded project 'CHEMFELLS IV' (No. CZ.02.2.69/0.0/0.0/20_079/0017899) for support. I. D. acknowledges the University of Chemistry and Technology Prague for specific research grant No. A2_FCHT_2021_053.

References

1 M. Zeng and Y. Li, *J. Mater. Chem. A*, 2015, **3**, 14942–14962.
2 Q. Lu, Y. Yu, Q. Ma, B. Chen and H. Zhang, *Adv. Mater.*, 2016, **28**, 1917–1933.
3 R. Gusmão, M. Veselý and Z. Sofer, *ACS Catal.*, 2020, **10**, 9634–9648.
4 Z. Wang, H. H. Wu, Q. Li, F. Besenbacher, Y. Li, X. C. Zeng and M. Dong, *Adv. Sci.*, 2020, **7**, 1901382.
5 T. Qin, Z. Wang, Y. Wang, F. Besenbacher, M. Otyepka and M. Dong, *Nano-Micro Lett.*, 2021, **13**, 1–34.
6 F. M. Oliveira, N. Antonatos, V. Mazánek, D. Sedmidubský, Z. Sofer and R. Gusmão, *FlatChem*, 2022, **32**, 100334.
7 S. Manzeli, D. Ovchinnikov, D. Pasquier, O. V. Yazyev and A. Kis, *Nat. Rev. Mater.*, 2017, **2**, 17033.
8 C. (Rose) Zhu, D. Gao, J. Ding, D. Chao and J. Wang, *Chem. Soc. Rev.*, 2018, **47**, 4332–4356.
9 H. Jin, C. Guo, X. Liu, J. Liu, A. Vasileff, Y. Jiao, Y. Zheng and S. Z. Qiao, *Chem. Rev.*, 2018, **118**, 6337–6408.
10 Z. Chen, X. Duan, W. Wei, S. Wang and B.-J. Ni, *J. Mater. Chem. A*, 2019, **7**, 14971–15005.
11 Z. Chen, D. Cummins, B. N. Reinecke, E. Clark, M. K. Sunkara and T. F. Jaramillo, *Nano Lett.*, 2011, **11**, 4168–4175.
12 H. Li, C. Tsai, A. L. Koh, L. Cai, A. W. Contryman, A. H. Fragapane, J. Zhao, H. S. Han, H. C. Manoharan, F. Abild-Pedersen, J. K. Nørskov and X. Zheng, *Nat. Mater.*, 2016, **15**, 48–53.

Open Access Article. Published on 11 April 2022. Downloaded on 2/8/2026 10:33:00 PM.
This article is licensed under a Creative Commons Attribution-NonCommercial 3.0 Unported Licence.

13 D. Voiry, H. Yamaguchi, J. Li, R. Silva, D. C. B. Alves, T. Fujita, M. Chen, T. Asefa, V. B. Shenoy, G. Eda and M. Chhowalla, *Nat. Mater.*, 2013, **12**, 850–855.
14 L. Cheng, W. Huang, Q. Gong, C. Liu, Z. Liu, Y. Li and H. Dai, *Angew. Chem., Int. Ed.*, 2014, **53**, 7860–7863.
15 S. Li, J. K. Lee, S. Zhou, M. Pasta and J. H. Warner, *Chem. Mater.*, 2019, **31**, 387–397.
16 E. Chen, W. Xu, J. Chen and J. H. Warner, *Mater. Today Adv.*, 2020, **7**, 100076.
17 K. Lasek, J. Li, S. Kolekar, P. M. Coelho, L. Guo, M. Zhang, Z. Wang and M. Batzill, *Surf. Sci. Rep.*, 2021, **76**, 100523.
18 S. Supriya, N. Antonatos, J. Luxa, R. Gusmão and Z. Sofer, *FlatChem*, 2021, **29**, 100280.
19 Y. Zhao, J. Qiao, Z. Yu, P. Yu, K. Xu, S. P. Lau, W. Zhou, Z. Liu, X. Wang, W. Ji and Y. Chai, *Adv. Mater.*, 2017, **29**, 1604230.
20 Y. Ma, X. Shao, J. Li, B. Dong, Z. Hu, Q. Zhou, H. Xu, X. Zhao, H. Fang, X. Li, Z. Li, J. Wu, M. Zhao, S. J. Pennycook, C. H. Sow, C. Lee, Y. L. Zhong, J. Lu, M. Ding, K. Wang, Y. Li and J. Lu, *ACS Appl. Mater. Interfaces*, 2021, **13**, 8518–8527.
21 Y. Wang, L. Li, W. Yao, S. Song, J. T. Sun, J. Pan, X. Ren, C. Li, E. Okunishi, Y.-Q. Wang, E. Wang, Y. Shao, Y. Y. Zhang, H. Yang, E. F. Schwier, H. Iwasawa, K. Shimada, M. Taniguchi, Z. Cheng, S. Zhou, S. Du, S. J. Pennycook, S. T. Pantelides and H.-J. Gao, *Nano Lett.*, 2015, **15**, 4013–4018.
22 R. A. B. Villaos, C. P. Crisostomo, Z.-Q. Huang, S.-M. Huang, A. A. B. Padama, M. A. Albao, H. Lin and F.-C. Chuang, *npj 2D Mater. Appl.*, 2019, **3**, 2.
23 J. Shi, Y. Huan, M. Hong, R. Xu, P. Yang, Z. Zhang, X. Zou and Y. Zhang, *ACS Nano*, 2019, **13**, 8442–8451.
24 S. Lin, Y. Liu, Z. Hu, W. Lu, C. H. Mak, L. Zeng, J. Zhao, Y. Li, F. Yan, Y. H. Tsang, X. Zhang and S. P. Lau, *Nano Energy*, 2017, **42**, 26–33.
25 D. Hu, T. Zhao, X. Ping, H. Zheng, L. Xing, X. Liu, J. Zheng, L. Sun, L. Gu, C. Tao, D. Wang and L. Jiao, *Angew. Chem., Int. Ed.*, 2019, **58**, 6977–6981.
26 L.-J. Ma and H. Shen, *Appl. Surf. Sci.*, 2021, **545**, 149013.
27 A. Ciarrocchi, A. Avsar, D. Ovchinnikov and A. Kis, *Nat. Commun.*, 2018, **9**, 919.
28 B. M. Szydłowska, O. Hartwig, B. Tywoniuk, T. Hartman, T. Stimpel-Lindner, Z. Sofer, N. McEvoy, G. S. Duesberg and C. Backes, *2D Mater.*, 2020, **7**, 45027.
29 A. Boudenne, L. Ibos, M. Fois, J. C. Majesté and E. Géhin, *Composites, Part A*, 2005, **36**, 1545–1554.
30 Z. Wang, Q. Li, F. Besenbacher and M. Dong, *Adv. Mater.*, 2016, **28**, 10224–10229.
31 H. Xu, H. Zhang, Y. Liu, S. Zhang, Y. Sun, Z. Guo, Y. Sheng, X. Wang, C. Luo, X. Wu, J. Wang, W. Hu, Z. Xu, Q. Sun, P. Zhou, J. Shi, Z. Sun, D. W. Zhang and W. Bao, *Adv. Funct. Mater.*, 2019, **29**, 1805614.
32 M. Yan, E. Wang, X. Zhou, G. Zhang, H. Zhang, K. Zhang, W. Yao, N. Lu, S. Yang, S. Wu, T. Yoshikawa, K. Miyamoto, T. Okuda, Y. Wu, P. Yu, W. Duan and S. Zhou, *2D Mater.*, 2017, **4**, 45015.
33 J. D. Benck, B. A. Pinaud, Y. Gorlin and T. F. Jaramillo, *PLoS One*, 2014, **9**, e107942.
34 D. C. Marcano, D. V. Kosynkin, J. M. Berlin, A. Sinitskii, Z. Sun, A. Slesarev, L. B. Alemany, W. Lu and J. M. Tour, *ACS Nano*, 2010, **4**, 4806–4814.
35 D. Bouša, K. Friess, K. Pilnáček, O. Vopička, M. Lanč, K. Fónod, M. Pumera, D. Sedmidubský, J. Luxa and Z. Sofer, *Chem. – Eur. J.*, 2017, **23**, 11416–11422.
36 E. Chen, W. Xu, J. Chen and J. H. Warner, *Mater. Today Adv.*, 2020, **7**, 100076.
37 M. O'Brien, N. McEvoy, C. Motta, J.-Y. Zheng, N. C. Berner, J. Kotakoski, K. Elibol, T. J. Pennycook, J. C. Meyer, C. Yim, M. Abid, T. Hallam, J. F. Donegan, S. Sanvito and G. S. Duesberg, *2D Mater.*, 2016, **3**, 21004.
38 C. Yim, K. Lee, N. McEvoy, M. O'Brien, S. Riazimehr, N. C. Berner, C. P. Cullen, J. Kotakoski, J. C. Meyer, M. C. Lemme and G. S. Duesberg, *ACS Nano*, 2016, **10**, 9550–9558.
39 P. Kuang, Y. Wang, B. Zhu, F. Xia, C. W. Tung, J. Wu, H. M. Chen and J. Yu, *Adv. Mater.*, 2021, **33**, 2008599.
40 C. M. A. Brett and A. M. O. Brett, *Electrochemistry: principles, methods, and applications*, Oxford Science Publications, Oxford, 1993.
41 S. Anantharaj, S. R. Ede, K. Karthick, S. Sam Sankar, K. Sangeetha, P. E. Karthik and S. Kundu, *Energy Environ. Sci.*, 2018, **11**, 744–771.
42 J. Song, C. Wei, Z. F. Huang, C. Liu, L. Zeng, X. Wang and Z. J. Xu, *Chem. Soc. Rev.*, 2020, **49**, 2196–2214.

© 2022 The Author(s). Published by the Royal Society of Chemistry